Shear-wave velocities from broadband HVSR measurements for geothermal resource assessment near Burwash Landing, Yukon

Fernando Berumen-Borrego[*], *Hersh Gilbert, Jan Dettmer,*
Jeremy M. Gosselin and Pejman Shahsavari
Department of Earth, Energy, and Environment, University of Calgary, Calgary, Alberta, Canada

Abstract

As Canada pursues net-zero CO_2 emissions targets, geothermal energy represents a promising solution, especially in northern Yukon communities such as Burwash Landing. Currently, Burwash Landing relies on importing diesel for power and heating and would benefit from a reliable source of renewable energy. Our study uses horizontal-to-vertical spectral ratio (HVSR) measurements from nine temporary broadband seismometers to refine shear-wave velocity models for the upper 500 m of the crust. These models constrain layering and structure within shallow sediments, depth to bedrock, and discontinuities within the bedrock. These results provide reliable estimates of the thickness of sedimentary cover overlying bedrock. Bedrock depths vary from 50 to 450 m, deepening to the northeast of the Denali fault, and follows a power-law increase with depth through sediments. These insights improve the geological understanding around this portion of the Denali fault and contribute to constructing comprehensive models for the development of geothermal energy in the region.

Introduction

Canada's commitment to net-zero CO_2 emissions by 2050 emphasizes the potential for geothermal energy to make a crucial contribution, especially for northern communities such as Burwash Landing, Yukon. Located along the Alaska Highway in southwest Yukon, the community of Burwash Landing is within the Traditional Territory of the *Lhù'àà̀n Mân' Ku Dań*, the Kluane Lake People, and home to the Kluane First Nation. Burwash Landing is located near the Denali fault, which is a crustal-scale, strike-slip fault and major geological terrane boundary (Colpron and Nelson, 2021). Geothermal gradients near Burwash Landing are estimated to be approximately 40°C/km (Witter, 2020). Both the seismogenic layer thicknesses and Curie point depth mapping (Li et al., 2017; Biegel et

al., 2023) suggest that the Denali and Duke River fault systems have elevated crustal temperatures and could potentially host viable geothermal resources (Li et al., 2017; Biegel et al., 2023). Based on the inferred geothermal gradient, temperatures near 40 to 45°C are expected at a depth of 1 km close to the Denali fault near Burwash Landing (Li et al., 2017; Biegel et al., 2023).

The Yukon Geological Survey (YGS) investigated this region to evaluate the potential for harnessing warm fluids near the surface (Witter, 2020; Finley et al., 2022; Tschirhart et al., 2022). This earlier work relied upon magnetotelluric (Tschirhart et al., 2022), gravity, magnetic, and low-frequency electromagnetic data

[*] fernando.berumenborr@ucalgary.ca

(Witter, 2020) to measure structural changes in the crust across the Denali fault (Fig. 1). However, the frequency ranges of the data and the scale of model resolution used in these studies were focused on structures at depths of approximately 0.2 to 1 km and greater. Our study contributes to this knowledge base by examining horizontal-to-vertical spectral ratio (HVSR) measurements from ambient seismic noise recorded by nine broadband seismometers that were deployed around Burwash Landing in summer 2021 (Fig. 1). The HVSR method is recognized for its effectiveness to infer shallow seismic velocity structures (Fäh et *al*., 2003; Arai and Tokimatsu, 2004; Havenith et *al*., 2007; Sánchez-Sesma et *al*., 2011; Cipta et *al*., 2018; Piña-Flores et *al*., 2021). The models presented here are based on a transdimensional Bayesian inversion to infer shear-wave velocity (V_S) beneath each station with associated uncertainties. The approach also avoids subjective model parameterization choices by allowing for the modelling of an unknown number of subsurface layers. This method increases the reliability and adaptability of our models (Dettmer et *al*., 2013; Cipta et *al*., 2018), a crucial feature given the limited geological data within the area. Our observations reveal significant variations in HVSR characteristics and basement depth across the Denali fault. Understanding these variations is crucial for refining our interpretations of the Denali fault and aids in refining interpretations from other geophysical methods. Additionally, we find that stations located on a thick sedimentary layer exhibit a power-law increase in V_S through this layer, a pattern observed in other basins and associated with sediment compaction and saturation (Scherbaum et *al*., 2003; Havenith et *al*., 2007; Molnar et *al*., 2010; Cipta et *al*., 2018).

Unlike its more seismically active central section in Alaska, the eastern extension of the Denali fault that extends through the Yukon, including near Burwash Landing, exhibits lower seismicity (Elliott and Freymueller, 2020). This makes seismic ambient noise methods such as HVSR particularly valuable. The approach was initially developed for seismic site effects studies (Kanai and Tanaka, 1961). The HVSR method has proven effective indicating ground shaking amplification during strong earthquakes that closely aligns with ambient noise estimates. Our work contributes new constraints on geological structures near Burwash Landing, which informs responsible geothermal resource development and natural (seismic) hazard mitigation.

Geological setting

The Denali fault, a large Cenozoic dextral strike-slip fault, extends more than 2100 km from northwestern British Columbia to southwestern Alaska, and plays a central role in interactions between the Insular and Intermontane superterranes (*e.g.*, Gabrielse et *al*., 2006; Elliott and Freymueller, 2020; Colpron and Nelson, 2021). The eastern segment of the Denali fault exhibits both strike-slip and reverse motions, as revealed by earthquake focal mechanism estimates (Gosselin et *al*., 2023). Displacement estimates for the Denali fault range from 370 to 480 km during the Cenozoic (Lowey, 1998; Waldien et *al*., 2021).

Near Burwash Landing, northeast of the Denali fault, basement rocks correspond to the Upper Cretaceous Kluane Schist, consisting of a quartz-mica schist with serpentinite and carbonate inclusions. This unit transitions from greenschist to lower amphibolite facies northwestward (Mezger et *al*., 2001; Israel et *al*., 2011). Southwest of the Denali fault, the basement comprises rocks from the Carboniferous to Upper Triassic Wrangellia terrane, which includes volcanic units of the Station Creek Formation and sedimentary units corresponding to the Hasen Creek Formation (Israel et *al*., 2005, 2006). These units are unconformably overlain by the Nikolai Basalt, which is unconformably overlain by marine clastic rocks of the Tatamagouche succession. The structural setting consists of various styles of folding and cut by steep faults, including the Denali fault, Duke River and Bock's Creek faults (Fig. 1; Israel et *al*., 2005, 2006). To the northeast of the Kluane Range, Quaternary to present sedimentary deposits accumulate and thicken toward Kluane Lake (Fig. 1; Kennedy, 2013).

Our HVSR-based study provides new insights into the depth to bedrock, offering a more detailed understanding of the thickness of the unconsolidated sedimentary layer, particularly in regions where well data are limited. For example, a well drilled to a depth of 384 m in Burwash Landing only encountered Quaternary sediments, whereas another well near station BL05 hit bedrock at a depth of 49 m. Comparing our HVSR results to these wells increases confidence in our shear-wave velocity models.
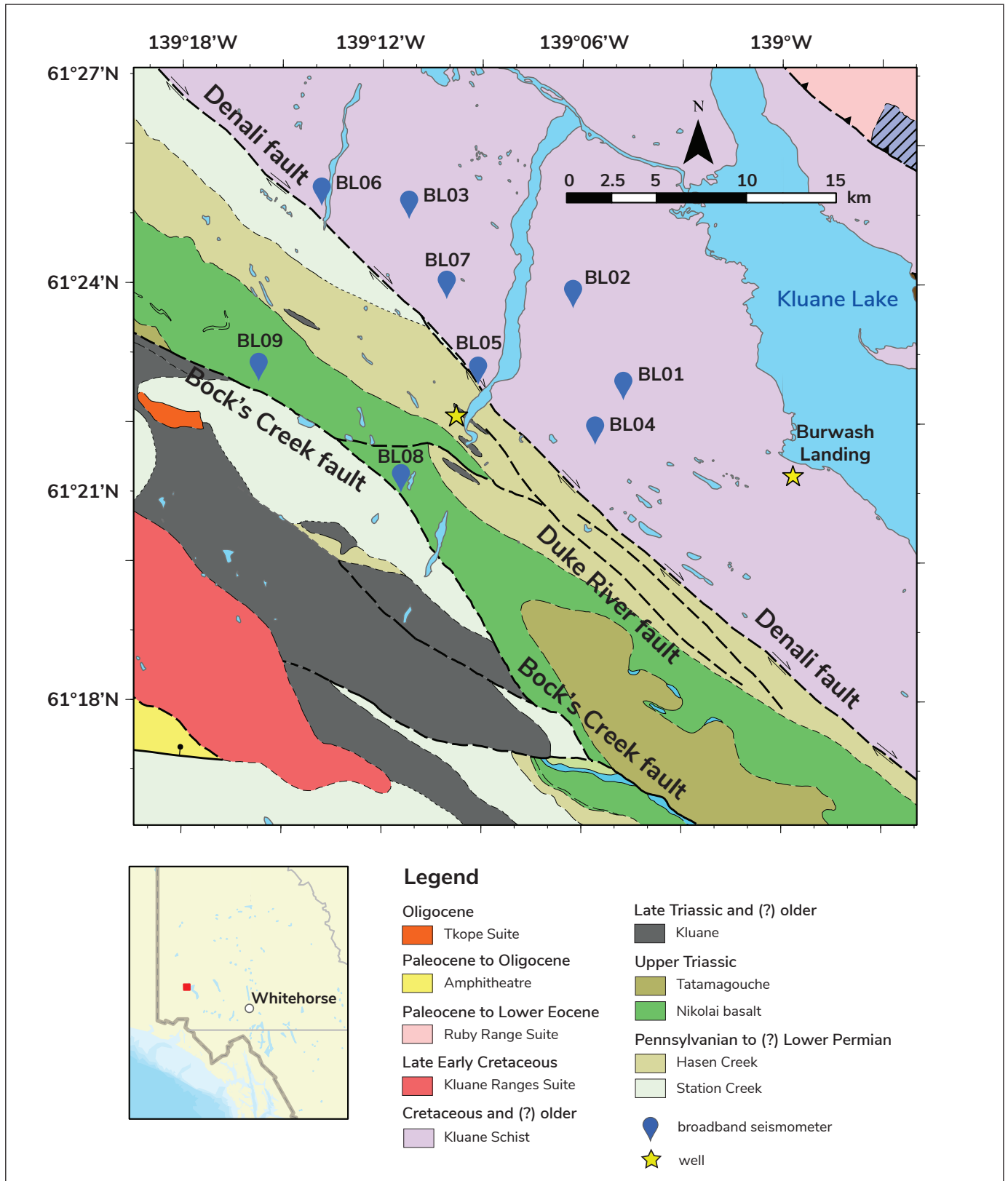
Figure 1. *Bedrock geology map of the Burwash Landing area (Colpron, 2022). Faults are shown by black dashed lines. Three-component seismometers are shown as blue pins. Wells drilled near the Duke River fault and Burwash Landing are shown as yellow stars.*

Horizontal-to-vertical spectral ratio method and data processing

The horizontal-to-vertical spectral ratio (HVSR) method, popularized by Nakamura (1989, 2008, 2019), is recognized for its efficiency in field acquisition and simplicity in processing ambient seismic noise. This noise, encompassing low-frequency signals from natural origins such as storms and ocean waves, and higher-frequency signals from anthropogenic activities, is a useful source for creating site-specific, shear-wave velocity profiles (Bonnefoy-Claudet et al., 2006). The lowest frequency peak observed on HVSR curves corresponds to the fundamental resonance frequency, f_0, at each site. Assuming HVSR is representative of resonance of horizontally polarized shear waves, the fundamental resonance frequency can be related to the shear velocity at the site by $f_0 = V_S / 4h$, where V_S is the average shear-wave velocity of the sedimentary column and h is its thickness (Nakamura, 2008, 2019). Recent studies suggest HVSR is attributed to, and can be modelled as, the ellipticity of ground motion caused by Rayleigh (surface) wave propagation (e.g., Cipta et al., 2018), or by a combination of these wave phenomena (Sánchez-Sesma et al., 2011; Molnar et al., 2022).

The HVSR curves are computed by taking the square-root of the product of the Fourier amplitude spectra of the north-south and east-west components ($H_{NS}(\omega)$ and $H_{EW}(\omega)$) and dividing them by the Fourier spectrum of the vertical component ($V(\omega)$), as expressed by

$$HVSR(\omega) = \frac{\sqrt{H_{NS}(\omega) \times H_{EW}(\omega)}}{V(\omega)}. \qquad (1)$$

Our HVSR measurements involve the following steps: defining an appropriate time window length; applying smoothing techniques to individual time windows; averaging horizontal spectra; removing noisy windows; and completing spectral ratio computations. This conventional processing using SESAME (Site EffectS assessment using AMbient Excitations) geophysics ensures both reliability and scientific rigour (SESAME, 2004). We used the open-source hvsrpy software (Vantassel, 2020) because of its capability to process multiple stations in parallel over several days, as well as its ability to reject time windows based on frequency-domain analysis (Cheng et al., 2020; Cox et al., 2020).

Individual time windows should be at least 10 times longer than the fundamental resonance period at a specific site (SESAME, 2004). The longest resonance period observed was approximately 3.25 s long beneath station BL07. Therefore, an entire day of data was used, segmented into time windows of 180 s each, yielding a total of 480 windows to ensure statistically meaningful results. Our choice of window length balances the need for spectral resolution and reliable statistics, enabling low resonance frequencies to be analyzed. The use of 480 windows exceeds the 20-window minimum suggested by Picozzi et al. (2005).

The logarithmic frequency-sampled smoothing filter proposed by Konno and Ohmachi (1998) was applied to minimize spectral variance. For the filter coefficient, we followed recommendations from SESAME (2004) and Cox et al. (2020) and used a value of 40. The geometric mean was used for averaging the horizontal spectra. The geometric mean tends to yield the least biased estimates, and its stability increases as the number of time windows grows (Cox et al., 2022; Molnar et al., 2022).

We used the frequency-domain window-rejection algorithm included in hvsrpy for effective time-window selection (Cox et al., 2020). The algorithm iteratively removes windows that deviate from a computed average frequency by more than a specified number of standard deviations. In this study, the rejection threshold was set at 1.75 standard deviations to preserve a reasonable number of time windows and eliminate significant outliers.

The final step in our HVSR processing involves the computation of mean μ and standard deviation σ of HVSR curves. The software hvsrpy uses log-normal statistics to compute these curves. Let ω denote a sampled frequency, and n be the number of time windows considered. For a given ω, the mean and standard deviation of HVSR at each frequency are calculated as

$$\mu(n, \omega) = exp^{\left(\frac{1}{n}\sum_{i=1}^{n} \ln(HVSR(\omega))\right)} \qquad (2)$$

and

$$\sigma_\omega(n, \omega) = \sqrt{\frac{1}{n-1}\sum_{i=1}^{n}(\ln(HVSR(\omega)) - \ln(\mu(n, \omega)))^2}. \qquad (3)$$

Once these values are determined, *hvsrpy* outputs $\mu(n, \omega)$, as well as the upper and lower bound curves, are calculated using

$$\mu \pm \sigma \,(n, \omega) = exp^{\left(\ln(\mu(n,\omega)) \pm \sigma_\omega(n,\omega)\right)}. \qquad (4)$$

This approach assumes that the natural logarithm of the HVSR values at different frequencies follow a normal distribution and are independently and identically distributed. An advantage of *hvsrpy* is its ability to output the standard deviation of the mean HVSR curve. The measure of the standard deviation of the HVSR curve allows for the incorporation of noise level estimates in the subsequent transdimensional inversion (Dettmer et a*l.*, 2013; Dosso et a*l.*, 2014; Cipta et a*l.*, 2018).

Our HVSR curves all feature a prominent peak corresponding to the f_0 beneath each station (Fig. 2b–d). Based on the frequency of these peaks, we classified the stations into three groups that show a strong correlation with depth to bedrock (Fig. 2a–d). Group one, comprising stations BL01, BL02, BL03, BL04 and BL07, exhibits low-frequency peaks ranging from approximately 0.3 to 0.4 Hz with amplitudes between approximately 1.8 and 3.5. These stations are situated to the northeast of the Denali fault, where a thick layer of sediments extends beyond a depth of 384 m at the well drilled in Burwash Landing. Group two, including stations BL05 and BL06, exhibit peaks at approximately 7.5 Hz with amplitudes under 2.5, indicative of a thinner sediment layer near the Denali fault, as confirmed by the well drilled near the Duke River. Lastly, group three, featuring stations BL08 and BL09, show peaks around 11 Hz with amplitudes of approximately 2.5, and are situated near the Bock's Creek fault.

Transdimensional inversion

To effectively solve non-linear inversion problems and include uncertainty quantification, we use Bayesian inference. Within the Bayesian framework, the solution to the inverse problem is given by the posterior probability density (PPD) of model parameters, which are connected by Bayes' theorem to the likelihood function—the probability to observe the data given a certain model—and a *priori* information, which is data independent, such as model parameterization. For nonlinear inverse problems, the PPD can be effectively

sampled using Markov chain Monte Carlo (MCMC) methods (Mosegaard and Tarantola, 1995; Dettmer et a*l.*, 2013; Cipta et a*l.*, 2018).

Spatial parameterization plays a crucial role in the ability of a model to accurately represent a system, particularly when model parameterization (e.g., number or thickness of layers) is not well known. Transdimensional inversions provide a robust approach to addressing this challenge. Instead of constraining to a unique parameterization, this method relaxes the selection to a set of parameterizations, avoiding subjective choices (Green 1995, 2003; Malinverno, 2002; Dettmer et a*l.*, 2013). This approach simultaneously considers multiple models, with a distinct number of layers and other parameters, while avoiding the need for explicitly specifying velocity structure and allowing for arbitrary layering.

In transdimensional methods, the PPD is commonly sampled using reversible-jump MCMC algorithms (Green, 1995, Dettmer et a*l.*, 2013; Dosso et a*l.*, 2014; Cipta et a*l.*, 2018). A structured strategy for parameterizing subsurface variations accommodating both smooth transitions and sharp discontinuities without explicit assumptions is used here (Bodin and Sambridge, 2009; Cipta et a*l.*, 2018). Models transition through the addition or subtraction of interfaces using a birth-death scheme (Geyer and Møller, 1994). For a birth step, an interface is created from a uniformly sampled depth, splitting a pre-existing layer. Elastic parameters for the new layer are randomly modified using a Gaussian distribution, centred on the current model state. Conversely, during death steps, interfaces are randomly eliminated, and the new state is randomly selected from one of the original layers. Elastic parameters also undergo perturbation steps using a Cauchy proposal targeting individual parameters leading to occasional large shifts, enhancing convergence rates (Dettmer et a*l.*, 2009).

To perform forward computations, we use the Geopsy tool (*gpell*) that computes Rayleigh wave ellipticity curves for homogeneous layered models (Wathelet et a*l.*, 2004; Wathelet, 2008). Attempting to match observed HVSR curves to these ellipticity calculations assumes that the HVSR peaks are exclusively due to Rayleigh wave ellipticity. Even though we expect this to be a valid assumption, any contribution to HVSR signals from other sources of energy, such as scattering
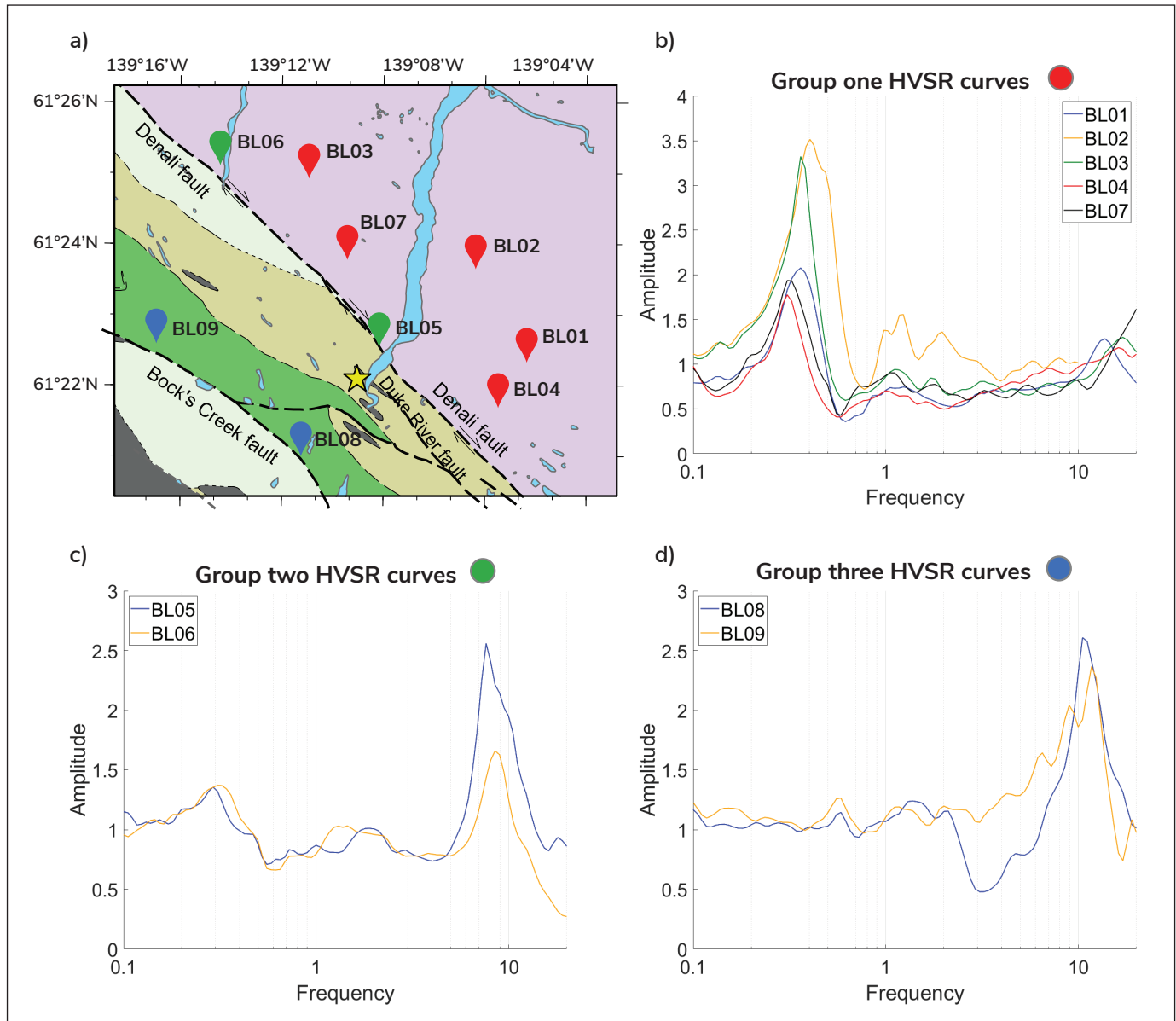
Figure 2. *Measured HVSR curves.* **a)** *Bedrock geology map denoting station locations, which are colour-coded based on their HVSR peak group classification. Group one stations are denoted by red pins, Group two stations with green pins, and Group three stations correspond to the blue pins. Subplots for each group show the corresponding HVSR curves* **b)–d)**.

or body waves, would not be accurately represented and would be a source of theory error in our analysis. We invert for the number of layers k as well as for V_S, V_P/V_S, ρ and thickness h in each layer. The log likelihood function of the history of the entire sampling chain was used to determine convergence for these inversions. Following Dettmer et al. (2013) and Cipta et al. (2018), the likelihood function is given by

$$L(\vec{d}|k,\vec{m}_k) = exp\left(-\frac{1}{2}(\vec{d}-\vec{d}(k,\vec{m}_k))^T C_d^{-1}(\vec{d}-\vec{d}(k,\vec{m}_k))\right). \quad (5)$$

We assume a Gaussian-distributed residual error distribution, which is a conservative choice supported by the central limit theorem. Here, $C_d = \sigma_\omega^2 * I$, where I is the identity matrix and σ_ω represents the standard deviation of the noise from equation 3, $d = [HVSR(\omega_0)$, $HVSR(\omega_1), ... , HVSR(\omega_i)]$. The modelled data vector, $\vec{d}(k,\vec{m}_k)$, reflects HVSR values at specific frequencies $\omega_0, \omega_1, ... , \omega_i$ for a given model.

Results

Our results demonstrate the effectiveness of transdimensional inversion of HVSR curves in determining shear-wave velocity profiles beneath broadband stations near Burwash Landing. These profiles, with reasonable uncertainties that increase with depth, align with the expected behaviour in diffusive wave fields such as Rayleigh wave propagation (Cipta et *al*., 2018). With minimal prior parameter information, the algorithm effectively models subsurface characteristics fitting observations within noise standard deviations (Fig. 3).

As described above, we categorized stations into three groups based on their HVSR curve resonance frequencies and proximity to the Denali fault (Fig. 2a–d). The models for station BL04 exhibited high uncertainty and poor resolution, likely due to hydrological effects because the water table was high (*i.e.*, near the surface) near this site. As a result, we do not report on BL04 further. Group one stations display low-frequency peaks (~0.3 to 0.4 Hz) with significant amplitudes (~1.8 and 3.5). This group comprises stations BL01, BL02, BL03, BL04, and BL07, situated over a thick section of Quaternary sediments (Fig. 4a–c, f and 5a–c, f). Here, we observed a distinct power-law increase in shear-wave velocity as a function of depth, which we attribute to sediment compaction. For instance, BL02 shows a gradual velocity increase from approximately 250 m/s to 600 m/s at 300 m depth, then a sharp transition to more than 1000 m/s, marking the boundary with the basement rocks. Station BL03 follows a similar pattern, with velocities rising from 250 to 900 m/s up to 400 to 420 m depth before jumping to approximately 1300 m/s. Station BL01 and BL07 reveal gradual velocity increases, and BL01 had a higher uncertainty in resolving bedrock depth. The sediment-bedrock interface depths vary within the group, emphasizing the lateral heterogeneity of the area and providing insights into its structural complexity.

Group two stations exhibit low-frequency peaks and higher frequencies of 7.75 and 7.51 Hz for stations BL05 and BL06, respectively. These stations are located over a package of thinner Quaternary sediments overlying bedrock (Fig. 4d, e and 5d, e). For BL05 and BL06, we noted power-law increases in velocity to approximately 700 m/s at depths of 90 to 100 m and 170 m, respectively, before sharply increasing to bedrock velocities of approximately 1000 to 1100 m/s. Another notable jump in velocity was observed within the bedrock to more than 2000 m/s at a depth of approximately 350 to 380 m.

Group three, comprising stations BL08 and BL09, presents single high-frequency peaks (~11 Hz) with amplitudes of approximately 2.5. The depth-to-bedrock estimates for these stations are about 1000 m for BL08 and 40 to 50 m for BL09 (Fig. 4g, h and 5g, h). Both stations exhibit gradual increases in velocity through the sediments, with sharp transitions to higher velocities in basement rocks. Station BL08 shows an increase to 700 m/s before a jump to approximately 1100 m/s, and another increase at approximately 260 m depth. The V_S profile for BL09 indicates a gradual increase to 500 m/s, then a sharp rise to 900 m/s at 40 to 50 m depth.

Our study across the station groups reveals varied patterns in shear-wave velocity changes through Quaternary sediments. Whereas a power-law increase in velocity due to compaction and/or saturation was observed for some stations, others exhibited more gradual velocity increases. Notably, at the sediment-bedrock interface, a sharp increase in velocity is seen consistently across the stations. Furthermore, the depth to this interface increases toward the northeast, reflecting sediment thickness variations in the region. These new constraints on the sediment-bedrock boundary, highlighted by the lateral heterogeneity observed across the station groups, are crucial for refining geological models of the region and aid in assessing geothermal potential. Reliable estimates of elastic properties in the shallow subsurface are necessary in enhancing the interpretation of other geophysical data, which often rely on initial (*i.e.*, starting) models (*e.g.*, Witter, 2020).

Discussion

Our results showcase the efficiency of HVSR transdimensional inversion in estimating the 1D velocity structure beneath stations near Burwash Landing. These estimates highlight significant variability in bedrock depth, ranging from 50 to 450 m, with depths sharply increasing to the northeast of the Denali fault. This approach proves effective even in areas with reduced seismicity and limited prior subsurface knowledge, such as the Burwash Landing region.
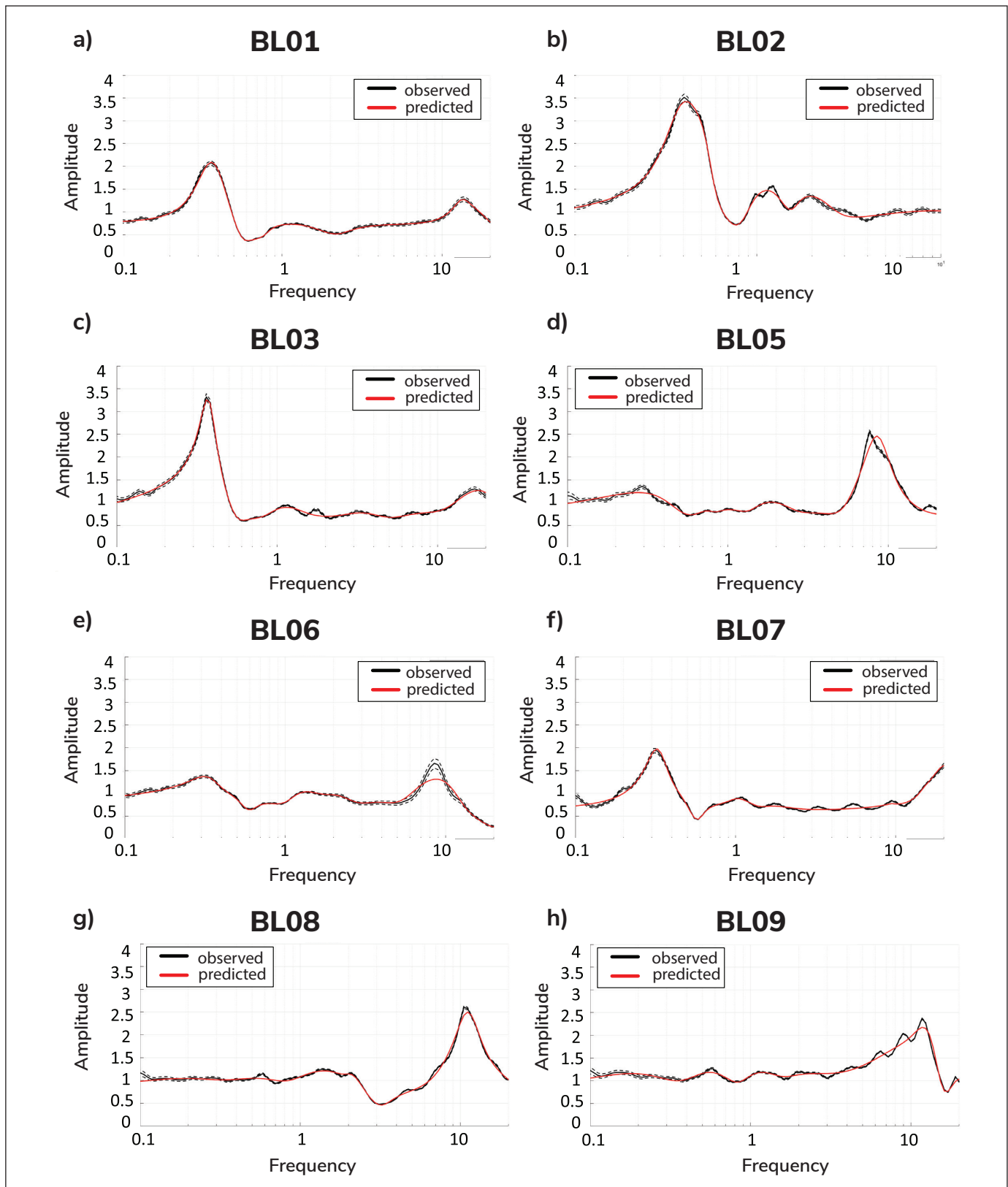
Figure 3. *Data fit curves.* **a)**–**h)** *Measured HVSR curves (solid black curves) and standard deviations (dashed black curves) are reasonably fit in all stations analyzed. The red curves show the HVSR for models with maximum a posteriori probability for stations BL01 to BL09.*
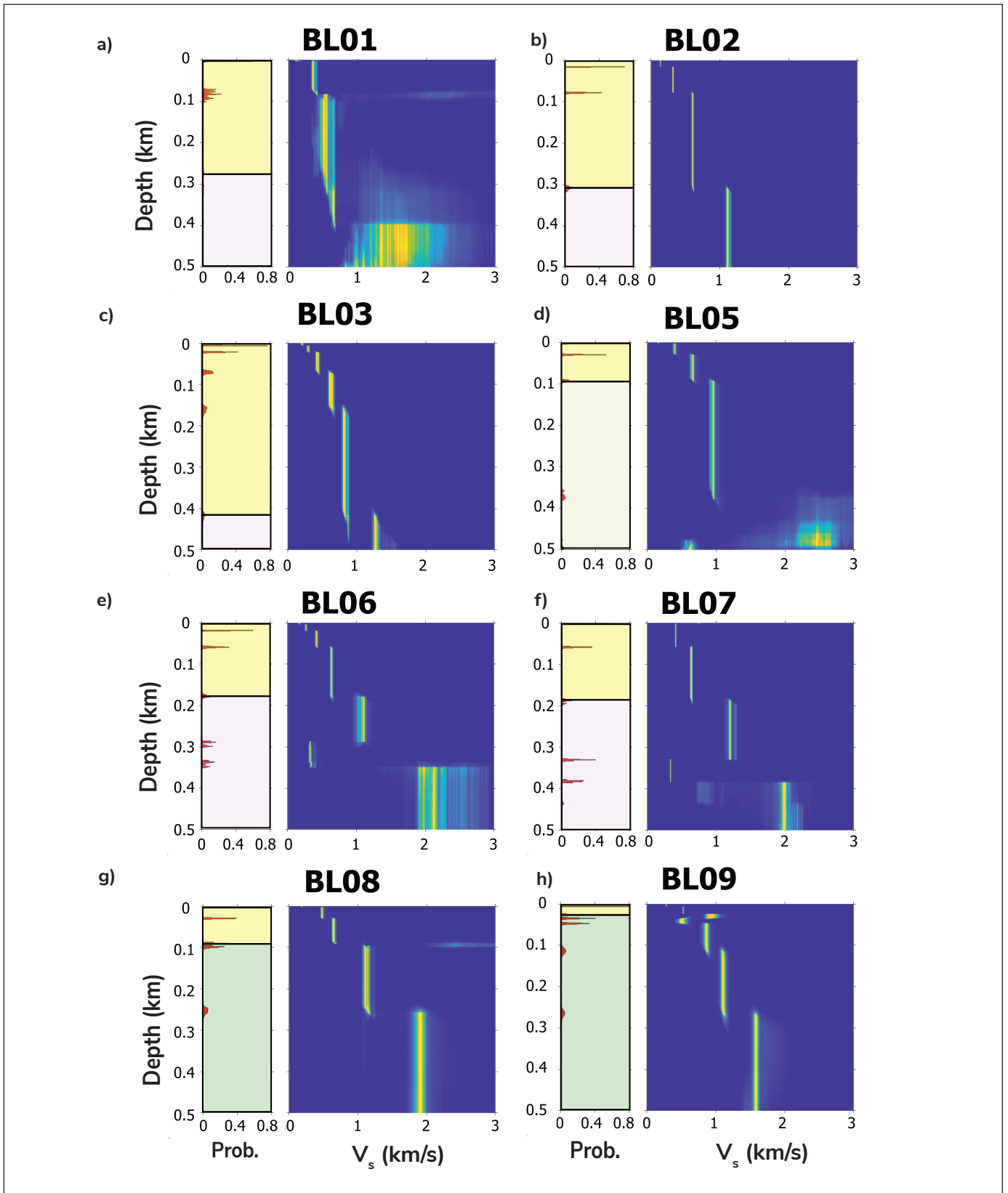
Figure 4. *Interface probability (left) and shear-wave velocity profiles (right) for the upper 500 m for stations BL01 to BL09* **a)**–**h)**. *The yellow shaded region in the interface probability plots is interpreted to correspond to sedimentary cover whereas the purple, brown and green mark the corresponding bedrock units as indicated in Figure 1.*
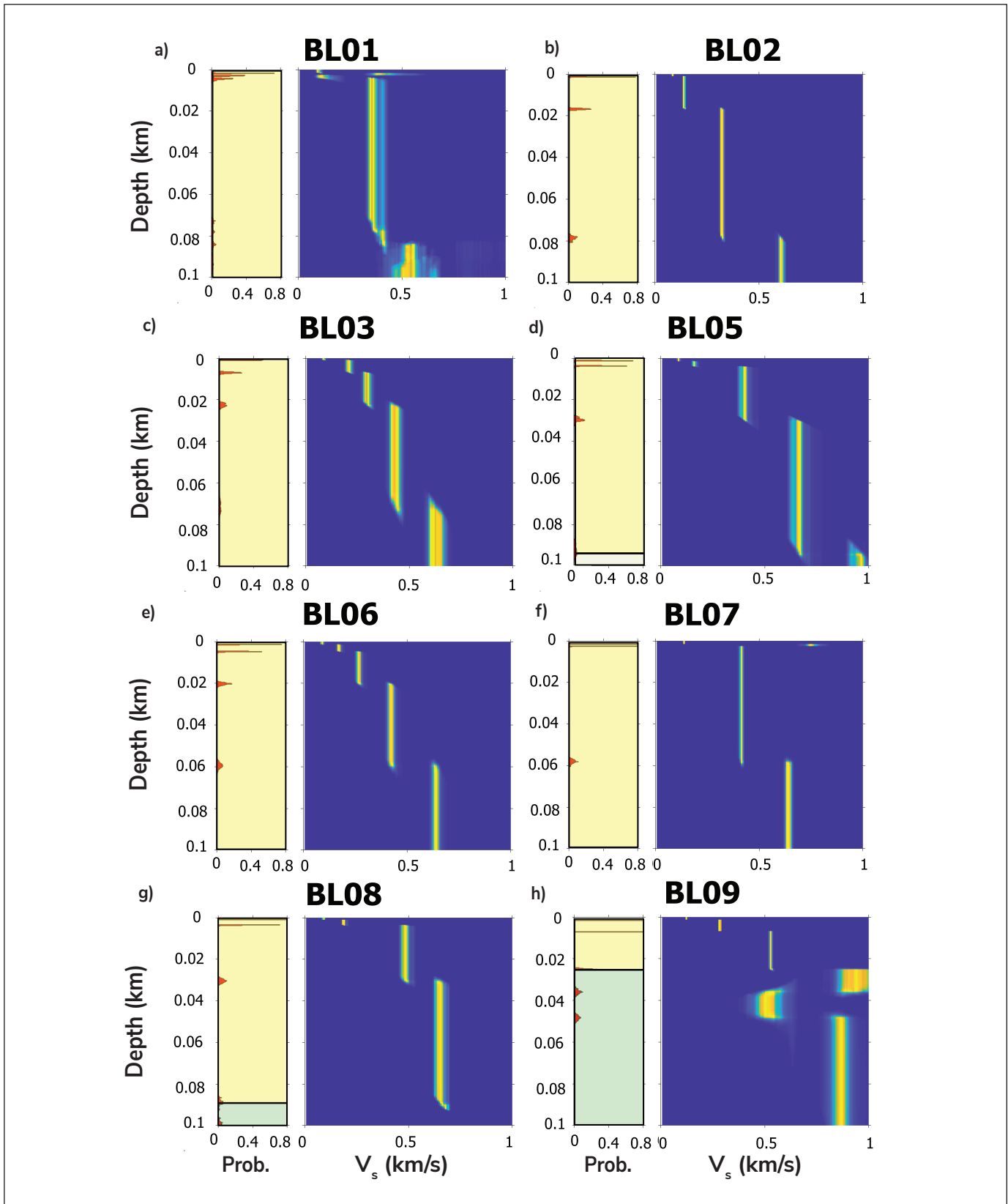
Figure 5. *Interface probability (left) and shear-wave velocity profiles (right) for the upper 100 m for stations BL01 to BL09* **a)**–**h)**. *The yellow shaded region in the interface probability plots is interpreted to correspond to sedimentary cover whereas the brown and green mark the corresponding bedrock units as indicated in Figure 1.*

A key aspect of our results is its agreement with the limited bedrock depth observations from nearby wells. For station BL05 near the Duke River fault, we have estimated bedrock to be close to 90 to 100 m deep. Our estimate of bedrock depth agrees with findings from drilling operations near this location in 2022 that encountered bedrock at a depth of only 49 m (M. Colpron, pers. comm., 2022). Earlier estimates of the depth to bedrock around BL05 used extremely low frequency – electromagnetics (ELF-EM), which suggested close to 200 m of overlying sediments at this location (Witter, 2020). For a gravity profile crossing the Denali fault (Fig. 1), Witter (2020) found that a model consisting of a layer of low-density sediments approximately 200 m thick atop a basement layer of increased densities fit the observed gravity variations well. Our HVSR results for this location indicate the presence of a shallow low V_S layer closer to approximately 100 m thick or less. These seismic constraints highlight the need to develop a revised model of the upper crust that can fit both the observed ELF-EM, gravity, magnetic and seismic observations while incorporating observational constraints from wells. Future efforts will be devoted to jointly modelling all available geophysical measurements to find a single model that can consistently match all observations.

Focusing on the upper 100 m, we find that at stations BL02, BL03, BL05, and possibly BL06, the pattern in which V_S increases with depth follows a power-law relationship between seismic velocities and depth (Fig. 5b–e). Seismic velocities exhibiting a power-law dependence on depths have been found in other sedimentary basins and have been attributed to sediment compaction or saturation. Scherbaum et al. (2003) inverted HVSR curves to determine shallow shear velocity profiles near Cologne, Germany. Testing inversions using a model in which seismic velocities are parameterized to follow a power-law increase with depth, this study found velocities that agree well with observations based on downhole measurements (Scherbaum et al., 2003). Using HVSR and dispersion curves, Havenith et al. (2007) observed a similar power-law increase in V_S within a basin of the Upper Rhine Graben while investigating the region bordering Switzerland, France and Germany. More recently, Molnar et al. (2010) used a Bayesian approach to estimate shear-wave velocities near Vancouver, British Columbia, from dispersion curves and found that a V_S profile parameterized using a power-law gradient to a

depth of at least 110 m fit observations from the Fraser River delta.

The differing pattern of sediment V_S variations as a function of depth (i.e., presence of power-law depth trend) suggests differing shallow structure within the overburden underlying the different groups of stations. The abrupt changes in velocities observed at shallow depths of less than 100 m for BL08 and BL09 (Fig. 5g, h) are suggestive of a thin layer of sedimentary cover atop basement rocks with faster V_S. The sediments within the thin shallow layer may not be subjected to sufficiently high pressures to be compacted so that the velocity of the layer increases, as observed for stations in group one.

The observed changes in shallow structures between the stations surrounding the Denali fault support earlier observations of structural changes at greater depths identified by other geophysical investigations of the region that used gravity and magnetic methods (Witter, 2020). Differences in V_S for the basement structures between stations in groups one, two and three provide support for variations in densities observed in gravity modelling across the boundary between the Kluane Schist and Station Creek Formation. Magnetotelluric observations provide further support for differences we observe in the shallow structure and suggest these extend to greater depths based on the identification of a conductive anomaly at depths greater than approximately 200 m to the northeast of the Denali fault (Tschirhart et al., 2022). Comparable to the lateral extent of stations in group one, this conductive anomaly extends from the Denali fault to the northeast. The alignment of these observations from diverse geophysical methods suggests that structural differences across the Denali fault extend from near-surface to depths of 1 km or more.

In summary, our study not only enhances the accuracy of depth to bedrock estimates but also provides insight into the sedimentary and tectonic dynamics, and the link to a deeper structure in the Burwash Landing area. The integration of HVSR results with other geophysical methods advances our understanding of geothermal resources in the area. Our work also underscores the adaptability of transdimensional inversion of HVSR curves. Despite sparse prior knowledge regarding the seismic structure in the Burwash Landing area, the transdimensional inversions provide estimates of shear-

wave velocities while avoiding subjective modelling choices. The incorporation of Bayesian inference is crucial, offering detailed uncertainty estimates and a more robust approach to non-linear problems compared to deterministic methods.

Conclusions

As part of a broader comprehensive geothermal investigation, we deployed nine broadband seismometers along the crustal-scale, right-lateral eastern Denali fault near Burwash Landing. Using data from this temporary network of seismic sensors, we have demonstrated that resonant frequencies of HVSR curves can be reliably fit using V_S models consisting of low-velocity layers atop higher-velocity basement, as suggested by Nakamura (1989, 2008, 2019). The velocity models presented here provide insights into the characteristics of the underlying geological structure near Burwash Landing. Our observations can be divided into three distinct groups based on their measured resonant frequency. We estimated depth to bedrock to be between 250 to 450 m below the surface for stations within group one with f_0 = ~0.3 to 0.4 Hz (Fig. 2b). For stations in group two, which exhibit f_0 = ~7.5 Hz (Fig. 2c), we estimated depth to bedrock to be approximately 90 to 100 m. Stations in group three, which exhibit f_0 >10 Hz (Fig. 2d), have depth to bedrock estimates of approximately 50 to 100 m. These new constraints of the shallow crust can contribute to refining the models produced using other geophysical methods (e.g., Witter, 2020; Tschirhart et al., 2022).

Several studies have emphasized the importance of incorporating higher order Rayleigh modes when fitting observed HVSR curves, particularly when low-velocity zones are present (Arai and Tokimatsu, 2004; Bonnefoy-Claudet et al., 2006). The joint inversion of HVSR curves and surface-wave dispersion curves has been used to mitigate the trade-off between layer thickness and velocity inherit to HVSR analysis (Parolai et al., 2005; Hobiger et al., 2012). Future efforts will be devoted toward integrating dispersion measured from a temporary, dense seismic array that was recently deployed in the region.

References

Arai, H. and Tokimatsu, K., 2004. S-wave velocity profiling by inversion of Microtremor H/V Spectrum. Bulletin of the Seismological Society of America, vol. 94, issue 1, p. 53–63. https://doi.org/10.1785/0120030028

Biegel, K., Gosselin, J. and Dettmer, J., 2023. Preliminary double-difference relocation earthquake catalogue for southwestern Yukon centred along the Denali fault zone. In: Yukon Exploration and Geology 2022, K.E. MacFarlane (ed.), Yukon Geological Survey, p. 1–18, plus digital appendices.

Bodin, T. and Sambridge, M., 2009. Seismic tomography with the reversible jump algorithm. Geophysical Journal International, vol. 178, issue 3, p. 1411–1436. https://doi.org/10.1111/j.1365-246x.2009.04226.x

Bonnefoy-Claudet, S., Cotton, F. and Bard, P.-Y., 2006. The nature of Noise Wavefield and its applications for site effects studies. Earth-Science Reviews, vol. 79, issue 3–4, p. 205–227. https://doi.org/10.1016/j.earscirev.2006.07.004

Cheng, T., Cox, B.R., Vantassel, J.P. and Manuel, L., 2020. A statistical approach to account for azimuthal variability in single-station HVSR measurements. Geophysical Journal International, vol. 223, issue 2, p. 1040–1053. https://doi.org/10.1093/gji/ggaa342

Cipta, A., Cummins, P., Dettmer, J., Saygin, E., Irsyam, M., Rudyanto, A. and Murjaya, J., 2018. Seismic velocity structure of the Jakarta Basin, Indonesia, using trans-dimensional Bayesian inversion of horizontal-to-vertical spectral ratios. Geophysical Journal International, vol. 215, issue 1, p. 431–449. https://doi.org/10.1093/gji/ggy289

Colpron, M. (compiler), 2022. Yukon Bedrock Geology Map. Yukon Geological Survey, Open File 2022-1, 1 000 000 scale map and legend.

Colpron, M. and Nelson, J.L., 2021. Northern Cordillera: Canada and Alaska. Encyclopedia of Geology (Second Edition), p. 93–106. https://doi.org/10.1016/b978-0-12-409548-9.12502-3

Cox, B.R., Cheng, T., Vantassel, J.P. and Manuel, L., 2020. A statistical representation and frequency-domain window-rejection algorithm for single-station HVSR measurements. Geophysical Journal International, vol. 221, issue 3, p. 2170–2183. https://doi.org/10.1093/gji/ggaa119.

Dettmer, J., Dosso, S.E. and Holland, C.W., 2009. Model selection and Bayesian inference for high-resolution seabed reflection inversion. The Journal of the Acoustical Society of America, vol. 125, issue 2, p. 706–716. https://doi.org/10.1121/1.3056553

Dettmer, J., Holland, C.W. and Dosso, S.E., 2013. Transdimensional uncertainty estimation for dispersive seabed sediments. Geophysics, vol. 78, issue 3. https://doi.org/10.1190/geo2012-0358.1

Dosso, S.E., Dettmer, J., Steininger, G. and Holland, C.W., 2014. Efficient trans-dimensional Bayesian inversion for geoacoustic profile estimation. Inverse Problems, vol. 30, issue 11, 114018. https://doi.org/10.1088/0266-5611/30/11/114018

Elliott, J. and Freymueller, J.T., 2020. A block model of present-day kinematics of Alaska and Western Canada. Journal of Geophysical Research: Solid Earth, vol. 125, issue 7. https://doi.org/10.1029/2019jb018378

Fäh, D., Kind, F. and Giardini, D., 2003. Inversion of local S-wave velocity structures from average H/V ratios, and their use for the estimation of site-effects. Journal of Seismology, vol. 7, issue 4, p. 449–467. https://doi.org/10.1023/b:jose.0000005712.86058.42

Finley, T., Salomon, G., Stephen, R., Nissen, E., Cassidy, J. and Menounos, B., 2022. Preliminary results and structural interpretations from drone lidar surveys over the Eastern Denali fault, Yukon. *In:* Yukon Exploration and Geology 2021, K.E. MacFarlane (ed.), Yukon Geological Survey, p. 83–105. https://doi.org/10.13140/RG.2.2.11124.01925

Gabrielse, H., Murphy, D.C. and Mortensen, J.K., 2006. Cretaceous and Cenozoic dextral orogen-parallel displacements, magmatism, and paleogeography, north-central Canadian Cordillera. *In:* Paleogeography of the North American Cordillera: Evidence For and Against Large-Scale Displacements, J.W. Haggart, R.J. Enkin and J.W.H. Monger (eds.), Geological Association of Canada Special Paper, vol. 46, p. 255–276.

Geyer, C.J. and Møller, J., 1994. Simulation Procedures and Likelihood Inference for Spatial Point Processes. Scandinavian Journal of Statistics, vol. 21, issue 1, p. 359–373.

Gosselin, J.M., Biegel, K., Hamidbeygi, M. and Dettmer, J., 2023. Improvements in the regional earthquake focal mechanism catalogue for southwestern Yukon. *In:* Yukon Exploration and Geology 2022, K.E. MacFarlane (ed.), Yukon Geological Survey, p. 63–76 plus digital appendices.

Green, P.J., 1995. Reversible jump Markov chain Monte Carlo Computation and Bayesian model determination. Biometrika, vol. 82, issue 4, p. 711–732. https://doi.org/10.1093/biomet/82.4.711

Green, P.J., 2003. Trans-dimensional Markov chain Monte Carlo Computation. *In:* Highly Structured Stochastic Systems, P.J. Green, N.L. Hjort and S. Richardson (eds.), p. 179–198. https://doi.org/10.1093/oso/9780198510550.003.0017

Havenith, H.-B., Fäh, D., Polom, U. and Roulle, A., 2007. S-wave velocity measurements applied to the seismic microzonation of Basel, Upper Rhine Graben. Geophysical Journal International, vol. 170, p. 346–358. https://doi.org/10.1111/j.1365-246X.2007.03422.x

Hobiger, M., Cornou, C., Wathelet, M., Giulio, G.D., Knapmeyer-Endrun, B., Renalier, F., Bard, P.-Y., Savvaidis, A., Hailemikael, S., Le, B.N., Ohrnberger, M. and Theodoulidis, N., 2012. Ground structure imaging by inversions of Rayleigh wave ellipticity: Sensitivity analysis and application to European Strong-motion sites. Geophysical Journal International, vol. 192, p. 207–229. https://doi.org/10.1093/gji/ggs005

Israel, S., Murphy, D., Bennett, V., Mortensen, J. and Crowley, J., 2011. New insights into the geology and mineral potential of the Coast Belt in southwestern Yukon. *In:* Yukon Exploration and Geology 2010, K.E. MacFarlane, L.H. Weston and C. Relf (eds.), Yukon Geological Survey, p. 101–123.

Israel, S., Tizzard, A.M. and Major, J., 2005. Geological Map of the Duke River Area (Parts of NTS 115G/2, 3, 5, 6, 7). Yukon Geological Survey Open File 2005–11.

Israel, S., Tizzard, A. and Major, J., 2006. Bedrock geology of the Duke River area, parts of NTS 115G/2, 3, 4, 6 and 7, southwestern Yukon. *In:* Yukon Exploration and Geology 2005, D.S. Emond, G.D. Bradshaw, L.L. Lewis and L.H. Weston (eds.), Yukon Geological Survey, p. 139–154.

Kanai, K. and Tanaka, T., 1961. On Microtremors VIII. Bulletin of Earthquakes Research Institute, vol. 39, p. 97–114.

Kennedy, K.E., 2013. Surficial Geology of Burwash Landing and Destruction Bay (parts of NTS 115G/2, 6 and 7) Yukon. Yukon Geological Survey Open File, 2013–14.

Konno, K. and Ohmachi, T., 1998. Ground-motion characteristics estimated from spectral ratio between horizontal and vertical components of microtremor. Bulletin of the Seismological Society of America, vol. 88, issue 1, p. 228–241. https://doi.org/10.1785/bssa0880010228

Li, C.-F., Lu, Y. and Wang, J., 2017. A global reference model of Curie-point depths based on EMAG2. Scientific Reports, vol. 7, article number 45129, https://doi.org/10.1038/srep45129

Lowey, G., 1998. A new estimate of the amount of displacement on the Denali Fault system based on the occurrence of carbonate megaboulders in the Dezadeash Formation (Jura-Cretaceous), Yukon, and the Nutzotin Mountains sequence (Jura-Cretaceous), Alaska. Bulletin of Canadian Petroleum Geology, vol. 46, issue 3, p. 379–386.

Malinverno, A., 2002. Parsimonious Bayesian Markov Chain Monte Carlo inversion in a nonlinear geophysical problem. Geophysical Journal International, vol. 151, issue 3, p. 675–688. https://doi.org/10.1046/j.1365-246x.2002.01847.x

Mezger, J.E., Chacko, T. and Erdmer, P., 2001. Metamorphism at a late Mesozoic accretionary margin: A study from the coast belt of the North American Cordillera. Journal of Metamorphic Geology, vol. 19, issue 2, p. 121–137. https://doi.org/10.1046/j.0263-4929.2000.00300.x

Molnar, S., Dosso, S.E. and Cassidy, J.F., 2010. Bayesian inversion of microtremor array dispersion data in southwestern British Columbia. Geophysical Journal International, vol. 183, p. 923–940. https://doi.org/10.1111/j.1365-246X.2010.04761.x

Molnar, S., Sirohey, A., Assaf, J., Bard, P.-Y., Castellaro, S., Cornou, C., Cox, B., Guillier, B., Hassani, B., Kawase, H., Matsushima, S., Sánchez-Sesma, F.J. and Yong, A., 2022. A review of the Microtremor horizontal-to-vertical spectral ratio (MHVSR) method. Journal of Seismology, vol. 26, issue 4, p. 653–685. https://doi.org/10.1007/s10950-021-10062-9

Mosegaard, K. and Tarantola, A., 1995. Monte Carlo sampling of solutions to inverse problems. Journal of Geophysical Research: Solid Earth, vol. 100, issue B7, p. 12431–12447. https://doi.org/10.1029/94jb03097

Nakamura, Y., 1989. A method for dynamic characteristics estimation of subsurface using microtremor on the ground surface. Railway Technical Research Institute, vol. 30, issue 1, p. 25–33.

Nakamura, Y., 2008. On the H/V Spectrum. The 14th World Conference on Earthquake Engineering, Beijing, China, 12–17 October 2008.

Nakamura, Y., 2019. What is the Nakamura method? Seismological Research Letters, vol. 90, issue 4, p. 1437-1443. https://doi.org/10.1785/0220180376

Parolai, S., Picozzi, M., Richwalski, S.M. and Milkereit, C., 2005. Joint inversion of phase velocity dispersion and H/V ratio curves from seismic noise recordings using a genetic algorithm, considering higher modes. Geophysical Research Letters, vol. 32, issue 1. https://doi.org/10.1029/2004gl021115

Picozzi, M., Parolai, S. and Richwalski, S.M., 2005. Joint inversion of H/V ratios and dispersion curves from seismic noise: Estimating the s-wave velocity of bedrock. Geophysical Research Letters, vol. 32, issue 11. https://doi.org/10.1029/2005gl022878

Piña-Flores, J., Cárdenas-Soto, M., Sarabia-González, A., García-Jerez, A., Sierra-Álvarez, C.A., Sáenz-Castillo, M.A., Luzón, F. and Sánchez-Sesma, F.J., 2021. Imaging the structure of the Sun Pyramid (Teotihuacán, Mexico) from passive seismic methods. Engineering Geology, vol. 281, no. 105969. https://doi.org/10.1016/j.enggeo.2020.105969

Sánchez-Sesma, F.J., Rodríguez, M., Iturrarán-Viveros, U., Luzón, F., Campillo, M., Margerin, L., García-Jerez, A., Suarez, M., Santoyo, M.A., and Rodríguez-Castellanos, A., 2011. A theory for Microtremor H/V spectral ratio: Application for a layered medium. Geophysical Journal International, vol. 186, issue 1, p. 221–225. https://doi.org/10.1111/j.1365-246x.2011.05064.x

Scherbaum, F., Hinzen, K.-G. and Ohrnberger, M., 2003. Determination of shallow shear wave velocity profiles in the Cologne/Germany area using ambient vibrations, Geophysical Journal International, vol. 152, p. 597–612.

SESAME, 2004. Guidelines for the Implementation of the H/V Spectral Ratio Technique on Ambient Vibrations: Measurements, Processing and Interpretation. SESAME European Research Project WP12 - Deliverable D23.12, European Commission – Research General Directorate Project No. EVG1-CT-2000-00026 SESAME, 62 p.

Tschirhart, V., Colpron, M., Craven, J., Ghalati, F.H., Enkin, R.J. and Grasby, S.E., 2022. Geothermal exploration in the Burwash Landing Region, Canada, using three-dimensional inversion of passive electromagnetic data. Remote Sensing, vol. 14, issue 23, no. 5963. https://doi.org/10.3390/rs14235963

Vantassel, J., 2020. jpvantassel/hvsrpy: latest (Concept). Zenodo. https://doi.org/10.5281/zenodo.3666956

Waldien, T.S., Roeske, S.M. and Benowitz, J.A., 2021. Tectonic underplating and dismemberment of the Maclaren-Kluane schist records Late Cretaceous terrane accretion polarity and ~480 km of Post-52 ma dextral displacement on the Denali fault. Tectonics, vol. 40, issue 10. https://doi.org/10.1029/2020tc006677

Wathelet, M., 2008. An improved neighborhood algorithm: Parameter conditions and dynamic scaling. Geophysical Research Letters, vol. 35, issue 9. https://doi.org/10.1029/2008gl033256

Wathelet, M., Jongmans, D. and Ohrnberger, M., 2004. Surface-wave inversion using a direct search algorithm and its application to ambient vibration measurements. Near Surface Geophysics, vol. 2, issue 4, p. 211–221. https://doi.org/10.3997/1873-0604.2004018

Witter, J., 2020. Early-stage exploration for geothermal energy resources along the Denali fault near Duke River, Yukon. Yukon Geological Survey, Open File 2020–3, 62 p.